UCLA
UCLA Previously Published Works

Title
Convective heat transfer and the pattern of thermal emission on the gas giants

Permalink

Journal

ISSN

Authors
Aurnou, Jonathan
Heimpel, Moritz
Allen, Lorraine
et al.

Publication Date

DOI

Convective heat transfer and the pattern of thermal emission on the gas giants

Jonathan Aurnou,[1] Moritz Heimpel,[2] Lorraine Allen,[3] Eric King[1] and Johannes Wicht[4]

[1]*Earth and Space Sciences, UCLA, 5690 Geology Bldg., Los Angeles, CA 90095-1567, USA. E-mail: aurnou@ucla.edu*
[2]*Department of Physics, University of Alberta, Edmonton, AB T6G 1V6, Canada*
[3]*Physics Division, US Coast Guard Academy, New London, CT 06320, USA*
[4]*Max Planck Institute for Solar System Research, 37191 Katlenburg-Lindau, Germany*

GJI Planetary science

SUMMARY

Jupiter and Saturn emit nearly twice the thermal energy they receive from the Sun. Although insolation decreases toward the poles, the large-scale outward heat flux is nearly uniform, with smaller-scale latitudinal undulations that correlate with the zonal jet streams. Here we present numerical models of rapidly rotating, turbulent 3-D convection in geometrically thin, uniformly forced layers of Boussinesq fluid that approximate the deep convection zones of Jupiter and Saturn. In previous studies we have demonstrated that such models generate zonal flows comparable to those observed on the gas giants. By analysing the simulated patterns of convective heat transfer, we show here that deep convection in the gas giants can explain the anomalously uniform large-scale thermal emissions as well as the jet-scale variations. In particular, we find that convective heat transfer by quasi-geostrophic thermal plumes in relatively thin spherical shell geometry generates an outward heat flow pattern with a broad equatorial minimum and peaks at the poles. The results suggest an alternative to the hypothesis that insolation controls the large-scale patterns of heat flux and zonal flow on the gas giants. Instead, we propose that the large-scale thermal and zonal flow fields originate deep within the planets' molecular envelopes.

Key words: Heat flow; Heat generation and transport; Planetary interiors.

1 INTRODUCTION

The thermal emission of a planet represents an admixture of interior heat and reradiated solar energy. Since the net outward heat flow exceeds solar deposition on both Jupiter and Saturn, a significant flux of heat must be escaping from the interior. Prior to the Pioneer missions, which measured Jupiter's thermal emission over 30 yr ago (Ingersoll *et al.* 1975; Ingersoll 1976), it was thought that the heat flux from the interiors of the giant planets would be spatially uniform. Making this assumption, Stone (1973) showed that solar energy deposition would result in an equator to pole temperature decrease of ∼10–30 K in the gas giant atmospheres. However, Pioneer 10 and 11 infrared observations showed that no significant latitudinal temperature gradients exist on Jupiter (Ingersoll *et al.* 1975). Subsequent space missions and ground based observations have confirmed that the total outward heat flow from the gas giants is roughly uniform in latitude, with smaller-scale undulations that resemble the structure of the jet-streams (Fig. 1a) (e.g. Hanel *et al.* 1981, 1983; Pirraglia 1984; Baines *et al.* 2007).

Because insolation is maximum near the equator and diminishes to nearly zero at the poles, some dynamical process, in the planetary interior or near the surface, must be responsible for the anomalous uniformity of the net emission. Previous explanations of the uni-

formly emitted heat flux have focussed on how solar heating may redistribute outward heat flow from the planetary interior, either through mixing in the outermost cloud layers (Conrath & Gierasch 1984; Pirraglia 1984; Williams 1985), or by giving rise to thermal gradients at depths that counterbalance the latitudinal insolation gradient (Ingersoll 1976; Ingersoll & Porco 1978).

Based on numerical modelling results (Heimpel *et al.* 2005; Heimpel & Aurnou 2007), we propose a novel explanation: that deep convection in the molecular envelopes of the gas giants, without solar forcing or tropospheric mixing effects, can generate heat flow that is strongest at the poles and weakest at the equator. As a result, the model's surface heat flow pattern, superimposed with that of solar energy deposition, is consistent with a roughly uniform net outward heat flow from Jupiter and Saturn. Such a pattern of convective heat transfer has not been found in earlier models of rapidly rotating spherical shell convection in which relatively weak zonal flows are generated (e.g. Gilman 1975, 1977; Christensen *et al.* 1999; Busse & Simitev 2006). In our rapidly rotating, turbulent convection models, a pattern of strong, alternating zonal jets arise. The zonal jet widths in our numerical models, and on Jupiter and Saturn, follow a Rhines' scaling theory (Heimpel & Aurnou 2007). Therefore, our results imply that deep convection can explain both the large-scale zonal flow and heat flux patterns observed on the gas giants.
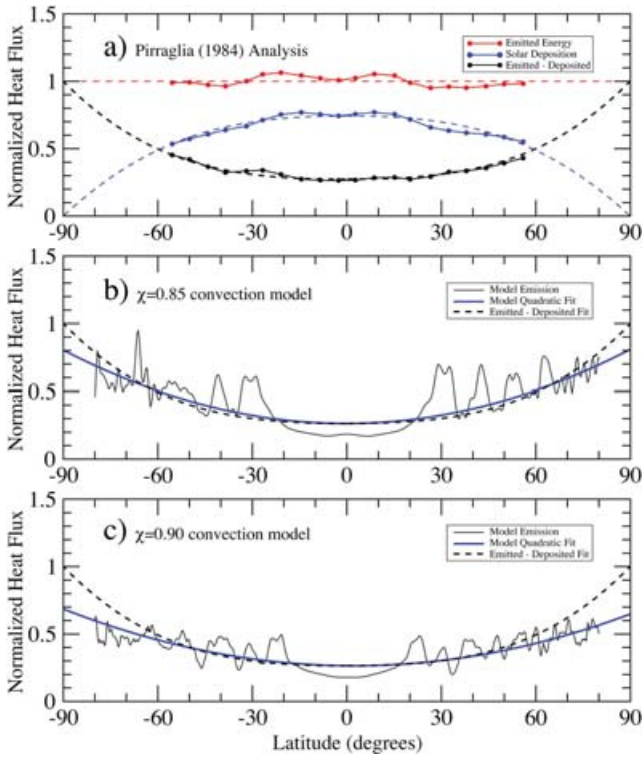
Figure 1. (a) Jovian thermal emission profiles normalized by the mean value of emitted thermal energy $\langle Q_o \rangle = 13.95$ W m^{-2} (adapted from Pirraglia 1984). Solid lines connect the data points that are demarcated by the filled circles; the dashed lines are extrapolations that fit the high latitude data from the Pioneer observations (Ingersoll *et al.* 1975). Red lines: net outward thermal emission. Blue lines: deposited solar energy. Black lines: difference between emitted and deposited solar energy. (b) $\chi = 0.85$ and (c) $\chi = 0.90$ model results. The solid black line shows the normalized, 10-rotation average of the outward thermal emission from the outer boundary of the $\chi = 0.85$ ($\chi = 0.90$) deep convection simulation at $t = 0.30217$ ($t = 0.13913$) viscous diffusion times. The solid blue line is the normalized quadratic fit to the model's emission. The dashed black line shows the emitted—deposited difference profile from (a).

The rest of the manuscript is organized as follows. In Section 2, we describe the numerical model used in this study. The detailed results of the calculation are discussed in Section 3. In Section 4, we discuss heat transfer mechanisms in our models and then apply our results to the gas giants, showing that the patterns of convective heat transfer can explain the uniformity of the thermal emission from Jupiter and Saturn.

2 NUMERICAL MODEL

We investigate convective heat transfer that develops in numerical models of 3-D, turbulent thermal convection in a rapidly rotating Boussinesq fluid by simultaneously solving, respectively, the Navier–Stokes equation, the energy equation and the continuity equation:

$$E\left(\frac{\partial \mathbf{u}}{\partial t} + \mathbf{u} \cdot \nabla \mathbf{u} - \nabla^2 \mathbf{u}\right) = -\nabla p - 2\hat{z} \times \mathbf{u} + \frac{RaE}{Pr}\left(\frac{\mathbf{r}T}{r_o}\right), \quad (1)$$

$$\frac{\partial T}{\partial t} + \mathbf{u} \cdot \nabla T = \left(\frac{1}{Pr}\right)\nabla^2 T, \quad (2)$$

$$\nabla \cdot \mathbf{u} = 0. \quad (3)$$

Here $\mathbf{u}$ is the velocity vector, T is the temperature and p is the non-hydrostatic pressure. The system of equations is non-dimensionalized using the spherical shell thickness $D = r_o - r_i$ for length scale, the viscous diffusion time $t = D^2/\nu$ for timescale, ν/D for velocity scale, $\rho\Omega^2 D^2$ for pressure scale and ΔT for temperature scale. The inner and outer shell boundaries are r_i and r_o, respectively; ν is the working fluid's kinematic viscosity; the shell's constant angular rotation velocity is Ω; and ΔT is the imposed temperature difference across the shell.

The calculations are performed with isothermal, free-slip boundary conditions and the gravitational acceleration varies linearly with radius. Each run is initialized in solid body rotation with angular rotation velocity $\Omega\hat{z}$, and the convection develops from a small, random temperature perturbation. The non-dimensional control parameters are the following:

Rayleigh number, $Ra = \dfrac{\alpha g_o \Delta T D^3}{\kappa \nu} = 5.56 \times 10^8$;

Ekman number, $E = \dfrac{\nu}{\Omega_o D^2} = 3.0 \times 10^{-6}$;

Prandtl number, $Pr = \dfrac{\nu}{\kappa} = 0.10$;

and radius ratios, $\chi = \dfrac{r_i}{r_o} = 0.85$ and 0.90,

where α is the thermal expansivity, g_o is gravitational acceleration on the outer boundary and κ is the thermal diffusivity. The Rayleigh number describes the ratio of buoyancy and diffusional effects; the Ekman number is the ratio of viscous and Coriolis forces; the Prandtl number is the ratio of thermal and viscous diffusion timescales; and the radius ratio describes the spherical shell geometry.

The models' spherical shell radius ratios, $\chi = 0.85$ and 0.90, shown schematically in Fig. 2(a), are thinner than in other recent rotating convection simulations of Jupiter and Saturn (Christensen 2002; Aurnou & Heimpel 2004). These radius ratio values correspond to bottom boundary depths that are significantly shallower than theoretical estimates of the transition depth to fully metallic hydrogen on the gas giants. Increasing electrical conductivity with depth in the molecular envelope will likely lead to dynamically significant Lorentz forces that will electromagnetically brake strong zonal flows at depths significantly shallower than the metallic hydrogen transition depth (Guillot *et al.* 2004). Thus, these radius ratio values approximate the estimated ranges for the depth of strong zonal flows on Jupiter and Saturn (Guillot 2005).

The Ekman number was chosen to be as low as is presently computationally feasible. Using the asymptotic scaling laws of Aubert *et al.* (2001) and Christensen (2002), the Rayleigh number was selected to obtain a zonal flow such that the peak non-dimensional velocity (the Rossby number, *Ro*) is comparable to those of the gas giants. Thus, while our simulations' *Ra* and *E* values are orders of magnitude from planetary values, the simulation seeks to approximate the large-scale fluid dynamics on the giant planets. With these choices of *Ra* and *E* it is not possible for our models to simultaneously match the absolute value of the thermal emissions from the gas giants. However, because our simulations are likely in the asymptotic regime (e.g. Aurnou 2007), we argue that the interaction between the convectively driven zonal flows and the convective heat transfer produces patterns of heat flow that are qualitatively similar to those observed on the gas giants.

These calculations are identical to the $\chi = 0.85$ and 0.90 cases whose zonal flow dynamics were studied by Heimpel & Aurnou (2007). The analyses presented in this paper are made with output from near the ends of the two integrations, at $t = 0.30217$ viscous
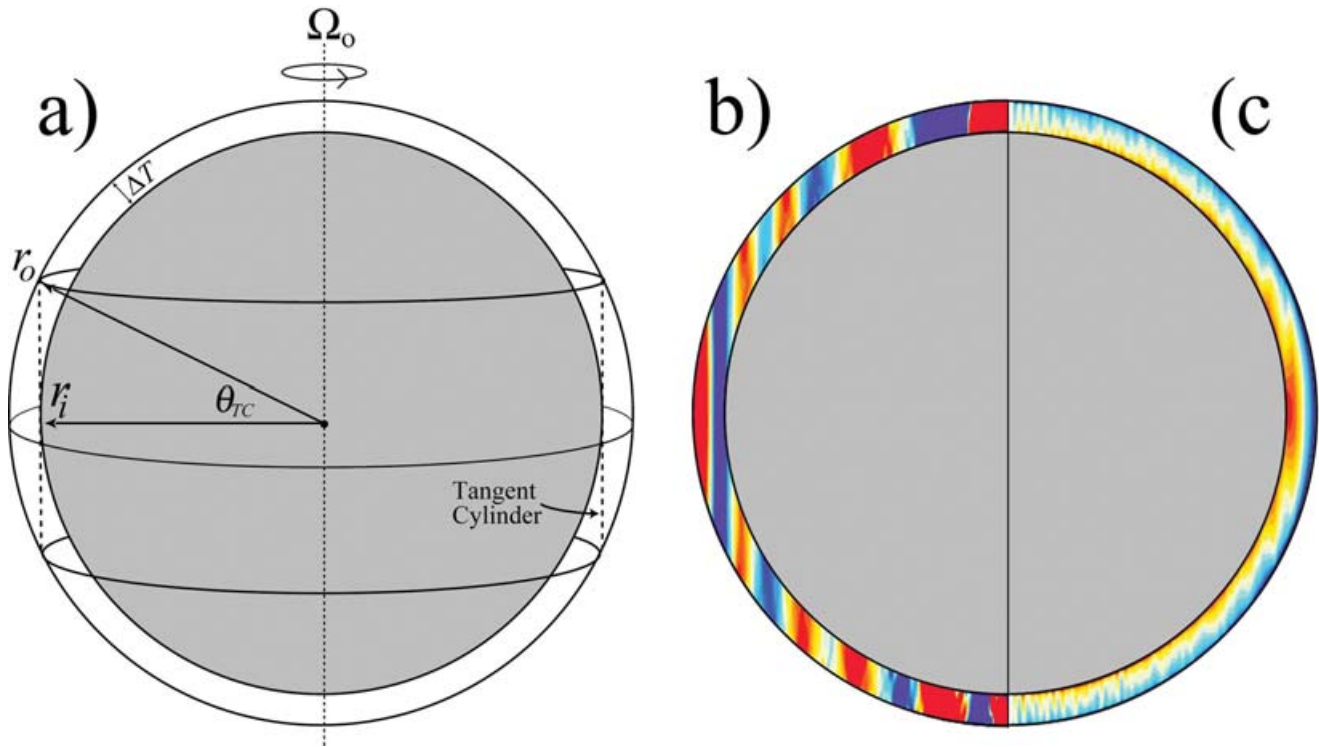
Figure 2. (a) Model schematic ($\chi = 0.90$): Rotating Boussinesq convection is driven by temperature differential ΔT between isothermal, free-slip boundaries r_i and r_o. The shell rotates at angular velocity Ω. The tangent cylinder, the imaginary axial cylinder that circumscribes the inner shell boundary, intersects the outer shell boundary at $\theta_{TC} = \pm\cos^{-1} \chi = \pm 25.8°$ latitude. The equatorial region is defined to be the fluid volume external to the tangent cylinder. Model results ($\chi = 0.90$): Meridional slice views of the azimuthally averaged (b) angular velocity and (c) temperature fields at $t = 0.13886$ viscous diffusion times.

diffusion timescales for the $\chi = 0.85$ case and at $t = 0.13913$ for the $\chi = 0.90$ case. In these calculations the spectral transform method, developed in the study of Glatzmaier (1984), is employed to solve simultaneously the Boussinesq Navier–Stokes and energy equations, using the MagIC formulation of Wicht (2002) and further outlined in Christensen & Wicht (2007). The governing equations are solved on 65 levels in the radial direction using a Chebychev polynomial representation. To efficiently time-step the solutions, the equations are solved on an azimuthally truncated spherical section with eight-fold symmetry and periodic boundary conditions on the bounding meridional planes (i.e. Al-Shamali *et al.* 2004). Within this truncated section, we use 512 points in latitude and 128 points in the eight-fold azimuthally truncated section (1024 azimuthal points in a full sphere) for the $\chi = 0.85$ model and 768 points in latitude and 192 points in the truncated azimuthal section (1536 azimuthal points in a full sphere) for the $\chi = 0.90$ model. For these grids, the maximum spherical harmonic degree, l_{max}, is 336 and 512 for the $\chi = 0.85$ and the $\chi = 0.90$ models, respectively. The flow field at latitudes greater than $\sim 80°$ is not well resolved in our models, possibly because the bounding meridional planes converge at the poles. Therefore, the modelling results will be disregarded between $80°$ and $90°$ latitude.

Even with the relatively large grids described above, we cannot resolve the full flow fields at the extreme parameter values employed. Thus, our simulations include viscous and thermal hyperdiffusivities that damp the solutions at the highest wavenumbers (Heimpel & Aurnou 2007). The hyperdiffusion parametrization is the following:

$$d(l) = d_o \left\{ 1 + \Lambda \left[\frac{(l+1) - l_{hd}}{(l_{max} + 1) - l_{hd}} \right]^{\beta} \right\}, \tag{4}$$

where $d(l)$ is the diffusivity that varies as a function of spherical harmonic degree l, d_o is the non-hyperdiffusive amplitude of the diffusivity, Λ is the amplitude of the hyperdiffusion, l_{hd} is the spherical harmonic degree at which the hyperdiffusion starts to act, and β is the hyperdiffusion exponent. In these calculations, we set $\Lambda = 1000$, $l_{hd} = 5$ and $\beta = 2$.

The key assumptions employed in our simulations are outlined herein, although we refer the reader to Heimpel *et al.* (2005) and Heimpel & Aurnou (2007) for further details of the model and numerical technique. We do not model tropospheric dynamics nor the effects of latitudinally varying solar energy deposition. Thus, the models' outer boundaries should be considered to lie below the maximum depth of solar energy deposition, corresponding to depths no shallower than about the 10 bar pressure level on the gas giants. We model convection only within the region where large-scale zonal flows are predicted to occur and we neglect the deeper electrically conductive regions where convection may be vigorous but zonal flows are likely to be weak (Guillot *et al.* 2004).

We employ isothermal boundaries (i) because they are numerically straightforward to implement and (ii) because Busse & Simitev (2006) have shown that convective heat transfer is not strongly affected by the choice of thermal boundary conditions in geodynamo simulations with free slip mechanical boundaries and Earth-like core geometry ($\chi = 0.4$). In addition, we use free-slip mechanical boundary conditions on both spherical shell boundaries, which allow us to model jovian-style alternating jets with the least computational expense (Danilov & Gurarie 2002; Aurnou & Heimpel 2004).

The working fluid in our model is Boussinesq, which means that it is incompressible except for the buoyancy effects of temperature perturbations (Tritton 1987). While the fluid in the interiors of the gas giants is compressible (Evonuk & Glatzmaier 2004; Guillot

Table 1. Nusselt number values, $Nu = $ total/conductive heat transfer, on the models' outer boundaries. The minimum values occur near the equator. The maximum values occur around the poles.

Model	Mean Nu	Min Nu	Max Nu
$\chi = 0.85$	3.7	2.0	6.0
$\chi = 0.90$	3.6	2.5	6.5

et al. 2004), the Boussinesq approximation allows us to model turbulent convective flow (rms Reynolds number $Re \sim 2 \times 10^4$) under quasi-geostrophic conditions (rms Rossby number $Ro \sim 0.01$). These high Re, low Ro conditions are likely characteristic of the adiabatically mixed molecular envelopes of the giant planets (Ingersoll & Pollard 1982; Liao *et al.* 2005). Thus, with Boussinesq fluid, we can simulate the first-order convective mixing processes that occur in the planetary interiors and, thereby, approximate their large-scale dynamics.

3 MODEL RESULTS

Fig. 1 shows the normalized outward heat flux from (a) Jupiter and our (b) $\chi = 0.85$ and (c) $\chi = 0.90$ models. The red line in Fig. 1(a) shows Jupiter's outward heat flux, which is approximately constant as a function of latitude (Pirraglia 1984). The blue lines, which peak at the equator and approach zero at the poles, denote the deposited solar energy. The black lines show the difference between the emitted energy and the solar deposition. This differential heat flux peaks at the poles and reaches a minimum in the equatorial region.

The solid black lines in Figs 1(b) and (c) show the normalized heat flux emanating, respectively, from the outer boundary of our $\chi = 0.85$ and 0.90 convection models. The solid blue lines in Figs 1(b) and (c) show the models' large-scale, outer boundary heat flux smoothed using a least-squares quadratic fit. The dashed black lines in Figs 1(b) and (c) show the differential heat flux pattern inferred for Jupiter in Fig. 1(a). Here we have normalized the model heat flux curves such that the quadratic fits and the differential heat flux are equal in value at the equator. The models' outward heat fluxes reach their minimum values at low latitudes and increase to their peak values at higher latitudes, approximating the inferred planetary heat flow patterns for the gas giants.

Table 1 show the values of the outer boundary Nusselt number, Nu. The Nusselt number is the total outward heat flow normalized by the conductive heat flow that would arise in the absence of convection. Thus, by definition, $Nu = 1$ in cases in which no convection occurs. In our models, the mean Nusselt number value is just less than 4. The peak values are close to 6 and occur near the poles; the minimum values, which occur around the equator, are near to 2.

Fig. 2 shows (a) the schematic structure of our $\chi = 0.90$ numerical model; meridional slices of its azimuthally averaged (b) angular velocity and (c) temperature fields. The azimuthally averaged angular velocity field in Fig. 2(b) shows that, due to the effects of rapid rotation, the turbulent flow organizes itself into large-scale, nested axial cylinders. The alternating east-west surface flows are the expression of these deep, quasi-geostrophic, cylindrical flows. A powerful prograde (eastward) jet dominates the shell's equatorial region, which is defined as the fluid lying outside the tangent cylinder shown in Fig. 2(a). At higher latitudes, alternating, smaller-scale zonal jets form. The jet widths follow topographic Rhines scaling for quasi-geostrophic turbulence in a spherical shell (Heimpel & Aurnou 2007).

Fig. 2(c) shows the azimuthally averaged temperature field. From this averaged thermal pattern, we infer that warm fluid convects more efficiently across the fluid layer at high latitudes in comparison to lower latitudes. This occurs because thermal plumes in the equatorial region buoyantly rise in cylindrical radius from the bottom boundary roughly half way across the fluid layer, but do not easily cross the outer half of the fluid layer. At higher latitudes inside the tangent cylinder, thermal plumes extend axially across the entire fluid layer. This difference between the polar and equatorial temperature fields explains the increased heat flux at higher latitudes in our models.

Close-ups and schematics from the $\chi = 0.85$ model are shown in Fig. 3. Heat transfer is inhibited in the equatorial region of the shell and generally grows stronger with increasing latitude. In the equatorial region (Figs 3a and b), local gravity is perpendicular to the planet's rotation axis. Thus, buoyant convective plumes travel in the $\hat{s}$-direction, outward from the rotation axis. As they do so, the plumes non-linearly interact with the zonal flow field, which causes them to deflect in the azimuthal $\hat{\phi}$-direction and lowers the $\hat{s}$-velocity at which they buoyantly rise across the fluid layer. This interaction dynamically inhibits the plumes' ability to cross the fluid layer and lowers the efficiency of convective heat transfer in the equatorial region of the shell. In the polar regions of the shell, in contrast, thermal plumes travel primarily in the axial $\hat{z}$-direction (Figs 3c and d). Since axial motions are not affected by the $\hat{z}$-independent zonal flows, polar plumes more efficiently convect heat across the shell.

Fig. 4 shows radial profiles of the azimuthally averaged temperature fields for the $\chi = 0.85$ (top row) and $\chi = 0.90$ models (bottom row). The solid (long-dashed) lines correspond to profiles from each model's northern (southern) hemisphere. The short-dashed lines show the temperature profile for purely conductive heat transfer (Kono & Roberts 2001):

$$T(r) = T_\mathrm{o} + \left[\frac{r_\mathrm{o} r_i}{r_\mathrm{o} - r_i} \left(\frac{1}{r} - \frac{1}{r_\mathrm{o}} \right) \right] \Delta T, \tag{5}$$

where T_o and $(T_\mathrm{o} + \Delta T)$ are the temperatures imposed, respectively, on r_o and r_i. The $\pm 70°$ latitude temperature profiles show that thermal boundary layers exist at both r_i and r_o and that the interior fluid is nearly isothermal. In the equatorial region, shown in the two rightmost panels, a thermal boundary layer forms only near r_i in the $\chi = 0.90$ case and the temperature profile does not greatly depart from the conductive state in the outer half of the shell. Thus, these profiles confirm that the convective heat transfer is well developed in the polar regions of the shell and becomes progressively weaker with decreasing latitude.

Fig. 5 shows the azimuthally averaged northern hemisphere temperature and angular velocity fields from (a) the $\chi = 0.85$ model and (b) the $\chi = 0.90$ model. The northern temperature field comprises the top half of each meridional slice. The northern hemisphere angular velocity field has been mirrored across the equator into the lower half of the slice. The vertical lines demarcate jet boundaries. Solid (dashed) lines mark the poleward (equatorward) boundaries of prograde jets. At low and mid-latitudes, convective heat transfer is inhibited across jet boundaries. In addition, warm (cold) fluid tends to build up on the equatorward (poleward) side of each mid-latitude jet, irrespective of jet direction. These intrajet temperature patterns cause the mid-latitude heat flux undulations in Figs 1(b) and (c). At higher latitudes, convective heat transfer occurs on axially aligned plume structures, which are approximately evenly distributed within each particular jet structure.
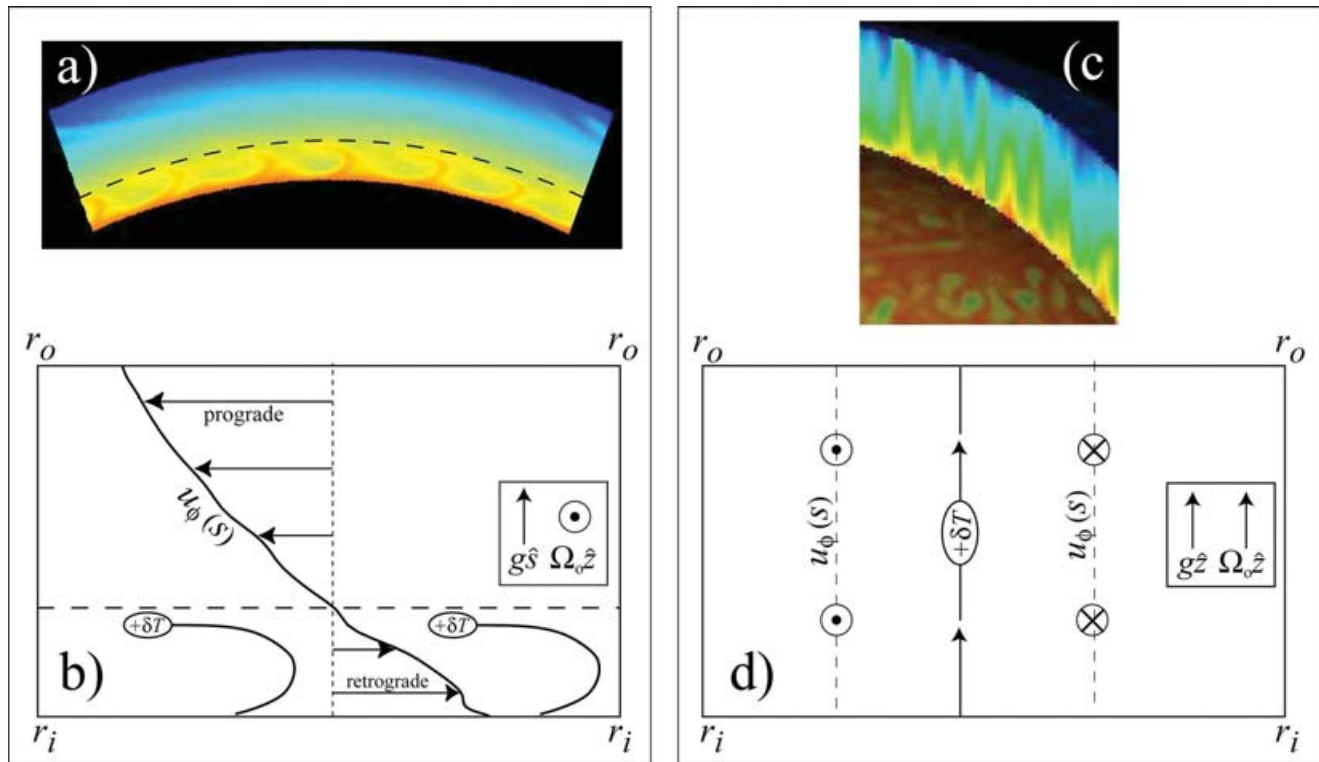
Figure 3. (a) Equatorial slice (the rotation axis points out of the page) of instantaneous isotherms showing strong azimuthal deflection of equatorial thermal plumes in the $\chi = 0.85$ case. The black long-dashed lines mark the boundary between the retrograde and prograde zonal jets. (b) Plan view schematic of a deflected thermal plumes in the equatorial region. The solid black line labelled $u_\phi(s)$ is the azimuthally averaged azimuthal velocity profile from the $\chi = 0.85$ case. The short-dashed vertical line marks the location of the jet boundary at $s = 0.897 r_o$. Note that the thermal plumes do not cross the boundary between the jets. (c) Close-up view of Fig. 2(c) showing a meridional slice of isotherms in the polar region of the $\chi = 0.90$ case. The lower spherical surface shows the temperature field just above r_i. In this image the rotation axis points upwards along the plane of the page. Red (blue) contours denote warm (cold) fluid. (d) Meridional slice schematic of a thermal plume in the polar regime.
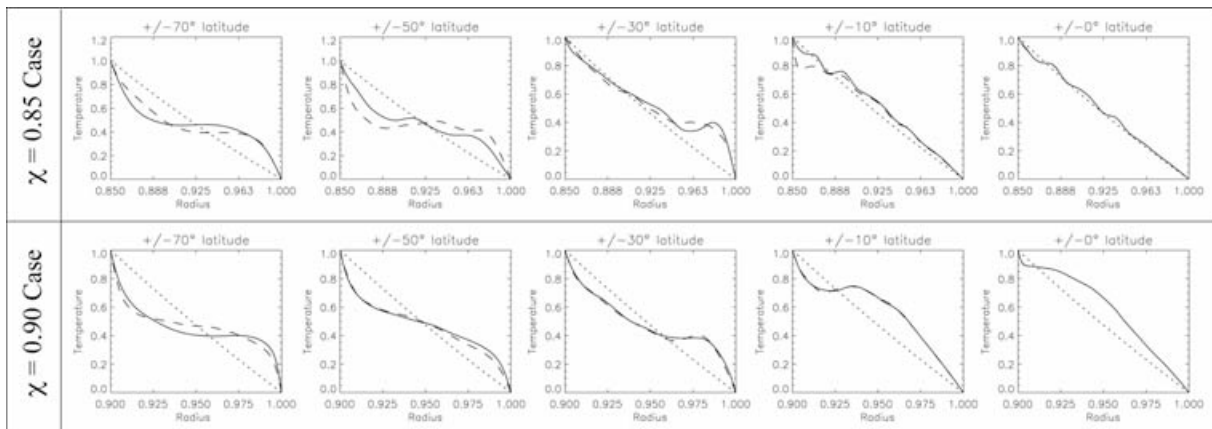

Figure 4. Azimuthally averaged temperature profiles plotted versus spherical radius, *r*, at five different latitude values. Solid (long-dashed) lines denote northern (southern) hemisphere profiles. Short-dashed lines denote the conductive temperature profile, given in (5). Top row: $\chi = 0.85$ case at $t = 0.30217$. Bottom row: $\chi = 0.90$ case at $t = 0.13913$.

4 DISCUSSION

4.1 Heat transfer dynamics

In studies of the solar convection zone, Gilman (1975, 1977) carried out some of the first detailed simulations of 3-D convection in a geometrically thin shell ($\chi = 0.80$). His earlier study investigated the linear regime for $E > 2 \times 10^{-3}$ and $Pr = 1$. The latter

study investigated non-linear convection for $E > 2 \times 10^{-3}$, $Pr = 1$ and $Ra \leq 4 \times 10^4$. In these simulations, the outer boundary heat flow has peak values at the equator and at the poles (also see Busse & Cuong 1977; Busse & Simitev 2006). The equatorial heat flux is driven by motion on columnar convection rolls that are aligned with the rotation axis (e.g. Roberts 1968; Dormy *et al.* 2004). The polar heat flux is carried by convection cells similar in structure to plane layer convection (Sreenivasan & Jones 2006). As the strength
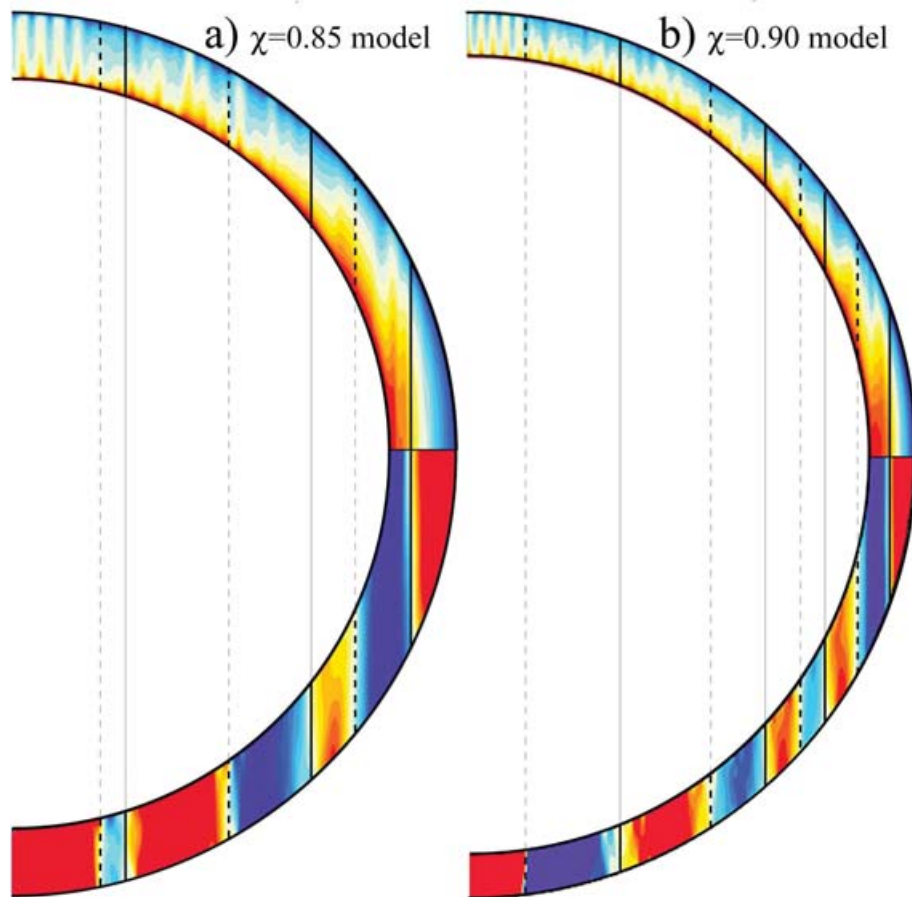
Figure 5. Meridional cuts of the northern hemisphere azimuthally averaged temperature (upper hemisphere) and angular velocity fields (lower hemisphere). (a) $\chi = 0.85$ case at $t = 0.30169$ and (b) $\chi = 0.90$ case at $t = 0.13886$. Solid (dashed) vertical lines mark the poleward (equatorward) prograde jet boundaries.

of rotation is increased, the equatorial heat flux remains strong at the inner boundary but weakens slightly at the outer boundary. This occurs because the convection columns become narrower in radial extent with increasing rotation rate. Because the columns form just outside the tangent cylinder, they still transport heat efficiently away from the inner boundary equator, but they no longer advect that heat directly to the outer boundary due to their limited lateral extent. At higher rotation rates, Gilman (1975) also finds that a significant flux of heat is transported in latitude towards the equator. This equatorward heat flux arises in more rapidly rotating cases in which the convection cells become columnar. The axially aligned columnar rolls transfer heat predominantly perpendicular to the rotation axis. Thus, warm fluid—transported cylindrically away from the inner boundary by the rolls—is carried equatorward; and cold fluid—transported cylindrically away from the outer boundary—is carried poleward.

The large-scale pattern of heat transfer in our present simulations differs from the patterns found in the moderate rotation rate, moderately supercritical, thin-shell cases of Gilman (1975, 1977). The large-scale pattern in our models arises mainly due to non-linear effects of strong quasi-geostrophic zonal flows on the heat transfer dynamics. Primarily, the zonal flows inhibit cylindrically radial motions of the thermal plumes. This preferentially limits heat transfer in the equatorial region of the shell, without affecting heat transfer at higher latitudes in our models.

In studies of rotating convection in spherical shell geometries, the effects of zonal flows on equatorial heat flow can be understood by comparing cases with stress-free and non-slip mechanical boundary conditions (e.g. Christensen *et al.* 1999; Aurnou & Olson 2001). In moderately supercritical cases with stress-free boundaries, stronger zonal flows develop and cylindrically radial motion of thermal plumes is inhibited. In constrast, zonal flows are weak in comparable cases with non-slip boundaries and thermal plumes travel in cylindrical radius across the shell, transporting warm fluid efficiently to the outer boundary in the shell's equatorial region. Similarly, strong magnetic fields can act to limit the formation of strong zonal flows in simulations of the geodynamo (e.g. fig. 10 in Kono & Roberts 2002). In such cases, it is found, again, that equatorial heat transfer is facilitated.

In rapidly rotating shells, axially aligned, columnar plumes tend to conserve potential vorticity (Aubert *et al.* 2003; Baldwin *et al.* 2007). The fluid's local value of potential vorticity (PV) varies due to two main components in a spherical shell of Boussinesq fluid: (i) local perturbations due to axial vorticity of fluid elements and (ii) spatial variations of background PV due to the axial column height variations in the spherical shell (e.g. Hide 1966; Heimpel & Aurnou 2007). Potential vorticity conservation causes convection columns in the equatorial region to become tilted in the prograde azimuthal direction as they travel outward in cylindrical radius. The prograde tilt of these columnar plumes generates
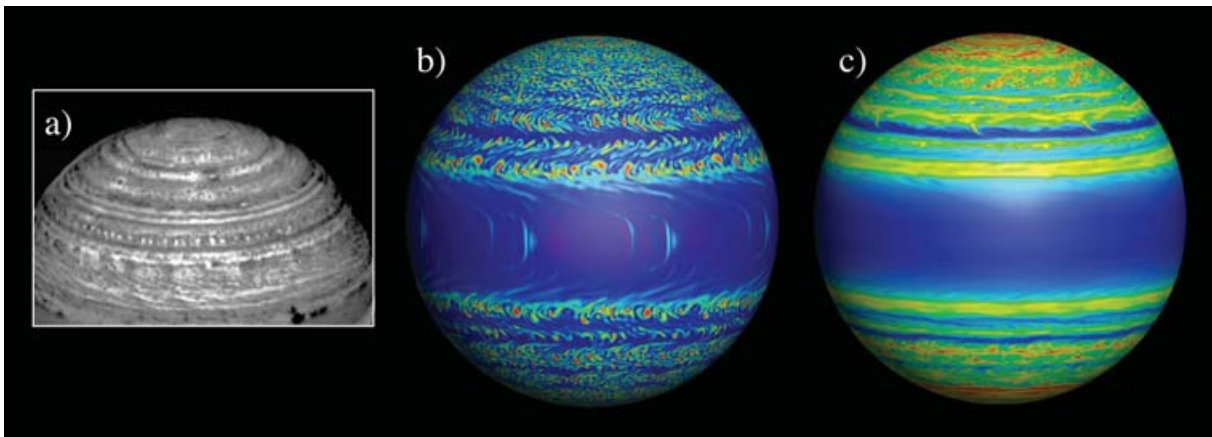
Figure 6. (a) Cassini/VIMS near IR image of Saturn contains latitudinal bands and intraband structures, such as the mid-latitude "string of pearls" pattern (adapted from http://wwwvims.lpl.arizona.edu). Rendered $\chi = 0.90$ modelling results: (b) Temperature field snapshot on the $r = 0.991r_o$ radial surface at $t = 0.13080$. (c) Temperature field averaged over ten rotations ending at $t = 0.12970$. Views in (b) and (c) are from $5°$ above the equatorial plane. Reds (blues) represents warm (cold) fluid. Each panel has its own colour scale.

non-linear Reynolds stresses that drive large-scale axially invariant zonal flows (Zhang 1992; Liao *et al.* 2007). Thus, kinetic energy of turbulent cylindrically radial motions, u'_s, is converted into kinetic energy of zonal motions. This conversion effectively decreases the cylindrical convective heat flux, $\langle u'_s T'\rangle$, which is the dominant component of convective heat transfer in the shell's equatorial region. In addition to this, sharp PV gradients are associated with strongly non-linear zonal jets (Marcus & Lee 1998). Such PV gradients act as local fluid barriers that further suppress cylindrically radial fluid motions (Baldwin *et al.* 2007). Thus, quasi-geostrophic zonal flows strongly modify the equatorial pattern of convective heat transfer.

At higher latitudes, the dominant component of convective heat transfer is axial, $\langle u'_z T'\rangle$. The high latitude heat transfer occurs via 3-D helical plumes (Aurnou *et al.* 2003; Sreenivasan & Jones 2006; Aubert *et al.* 2008). These polar plumes are not strongly affected by the axially invariant zonal flows and, thus, the mechanisms inhibiting equatorial heat transfer only weakly affect the heat transfer at high latitudes.

In our numerical models' the heat flow pattern associated with each individual mid-latitude jet features an equatorward local maximum and a poleward local minimum. This pattern develops because the mid-latitude quasi-geostrophic convection rolls within each jet preferentially transfer thermal anomalies perpendicular to the rotation axis—in cylindrical radius $\hat{s}$, similar to the mid-latitude heat transfer mechanism described in Gilman (1977). In regions where the boundaries are significantly inclined away from horizontal, this process drives warm fluid towards the equator and cold fluid towards higher latitudes. Because mixing tends to be inhibited across jet structures, warm (cold) fluid builds up on the equatorward (poleward) side of each mid-latitude jet. This same effect is not as strong at higher latitudes, where the boundaries approximate horizontal planes.

4.2 Planetary applications

The heat flux patterns in our models agree qualitatively with the inferred differential heat flow pattern on Jupiter (Fig. 1) and Saturn (Ingersoll *et al.* 2004). The models both have a large-scale increase in heat flux from equator to pole as well as smaller-

scale heat flux undulations that correlate with the structure of the smaller-scale mid-latitude jets. As shown in Fig. 6, the undulations in the mid-latitude thermal field in our model shares qualitatively similarities to banded near infrared images of Jupiter and Saturn (Ortiz *et al.* 1998; Orton & Yanamandra-Fisher 2005; Simon-Miller *et al.* 2006). In addition, deep convective plume tops in our models produce a mid-latitude temperature pattern that has structural similarities to the 'string of pearls' infrared features observed on Saturn by Cassini/VIMS measurements (Momary *et al.* 2006). Infrared images of Jupiter show a change from sheared structures at low latitudes to localized structures at higher latitudes (e.g. Baines *et al.* 2007). A similar change—from strongly sheared, low latitude structures to more localized, higher latitude axial plumes—occurs rather abruptly in the vicinity of the tangent cylinder in our models, as seen in Fig. 6(b).

These similarities suggest an alternative interpretation of the near infrared maps of the gas giants. The standard interpretation is that structures in these images result from cloud opacity variations acting on a uniform internal radiation field (i.e. Ortiz *et al.* 1998; Baines *et al.* 2005). In our models, it is found that the interior heat transfer pattern is not uniform, but instead has variations that are qualitatively similar in structure to the near infrared observations. Thus, we hypothesize that local regions of strong convective heat transfer are associated with cloud structures, similar to regions of convective upwelling in Earth's troposphere. This interpretation is qualitatively supported by the studies of Gierasch *et al.* (2000) and Sanchez Lavega *et al.* (2008), in which they argue, respectively, that deep convective plumes can account for a significant portion of Jupiter's interior heat flow and that deep plumes are important drivers of jovian zonal flows.

Because our models do not include a tropospheric layer, care must be taken in comparing our results with tropospheric observations of the gas giants. The outer boundary in our models should be thought of as lying well below the region where solar forcing effects occur, at pressures no less than roughly 10 bar. Taking this into account, our results are qualitatively consistent with the velocity data from the Galileo probe for pressures greater than approximately 5 bar. It should also be noted that thermal wind balance differs from that in a shallow tropospheric fluid layer (e.g. Vasavada & Showman 2005). In our models thermal wind balance corresponds to that of a

deep layer of fluid in which the thermal wind velocity, $\vec{U}_{TW}$, varies along the direction of the global rotation vector, $\hat{z}$, $\partial\vec{U}_{TW}/\partial z$. This is fundamentally different from thermal wind balance in a shallow troposphere. In a shallow fluid layer, thermal winds vary in the local radial direction $\hat{r}$ in proportion to the local radial component of the rotation vector, $\partial\vec{U}_{TW}/\partial r$. Thus, the $\hat{z}$-dependent thermal wind shears near the outer boundary of our models should not be directly compared to $\hat{r}$-dependent thermal winds that exist in the tropospheres of the gas giants.

Our modelling results suggest that deep convection on the gas giants is capable of producing an outward heat flux pattern that is minimal at the equator and maximal at the poles. When the heat flow pattern from our models is superposed with solar deposition, a quasi-uniform thermal emission pattern results. These convection models provide a self-consistent mechanism to explain the thermal emission on the gas giants. Furthermore, according to our models, the near uniformity of the thermal emission from the gas giants occurs because the ratio of solar deposition to internal emission is near unity. Thus, the uniformity depends on the planets' specific orbital properties. In contrast, if either tropospheric mixing smooths insolation and the interior heat flow is uniform (Stone 1973) or insolation controls the pattern of interior heat flow (Ingersoll & Porco 1978), then the thermal emission should remain uniform irrespective of the ratio of solar deposition to internal emission (i.e. irrespective of the planet's orbital properties). This fundamental difference may allow observers to test the validity of these hypotheses. For instance, since our models suggest that deep convective heat transfer is not strongly affected by solar energy deposition, the outward heat flow pattern due to deep convection should not change significantly over a given planet's orbital period. Thus, our models predict that observed secular variations in a planet's net outward heat flow will be dominated by seasonal changes in solar energy deposition (i.e. Nixon *et al.* 2007). This hypothesis is testable with high resolution thermal observations of the gas giants. Decisive, higher resolution measurements of Saturn can presently be made by the Cassini CIRS and VIMS instruments (e.g. Baines *et al.* 2005; Simon-Miller *et al.* 2006; Fletcher *et al.* 2007). Furthermore, NASA's proposed low altitude, polar orbiter, Juno, should be capable of discriminating whether the proposed coupling between outward heat flow and deep zonal flow occurs on Jupiter.

ACKNOWLEDGMENTS

REFERENCES

Al-Shamali, F.A., Heimpel, M.H. & Aurnou, J.M., 2004. Varying the spherical shell geometry in rotating thermal convection, *Geophys. Astrophys. Fluid Dyn.,* **98,** 153–169.

Aubert, J., Brito, D., Nataf, H.C., Cardin, P. & Masson, J.P., 2001. *Phys. Earth planet. Int.,* **128,** 51–74.

Aubert, J., Gillet, N. & Cardin, P., 2003. Quasigeostrophic models of convection in rotating spherical shells, *Geochem. Geophys. Geosys.*, **9**(7), doi:10.1029/2002GC000456.

Aubert, J., Aurnou, J.M. & Wicht, J., 2008. The magnetic structure of convection-driven numerical dynamos, *Geophys. J. Int.,* **172,** 945–956.

Aurnou, J.M., 2007. Planetary core dynamics and convective heat transfer scaling, *Geophys. Astrophys. Fluid Dyn.,* **101,** 327–345.

Aurnou, J.M. & Heimpel, M.H., 2004. Zonal jets in rotating convection with mixed mechanical boundary conditions, *Icarus,* **169,** 492–498.

Aurnou, J.M. & Olson, P.L., 2001. Strong zonal winds from thermal convection in a rotating spherical shell, *Geophys. Res. Lett.,* **28,** 2557–2559.

Aurnou, J.M., Andreadis, S., Zhu, L. & Olson, P., 2003. Experiments on convection in Earth's core tangent cylinder, *Earth planet. Sci. Lett.,* **212,** 119–134.

Baines, K.H. *et al.*, 2005. The atmospheres of Saturn and Titan in the near-infrared: first results of Cassini/VIMS, *Earth Moon Planets,* **96,** 119–147.

Baines, K.H. *et al.*, 2007. Polar lightning and decadal-scale cloud variability on Jupiter, *Science,* **318,** 226–229.

Baldwin, M.P., Rhines, P.B., Huang, H.-P. & McIntyre, M.E., 2007. The jet-stream conundrum, *Science,* **315,** 467–469.

Busse, F.H., 1970. Thermal instabilities in rapidly rotating systems, *J. Fluid Mech.,* **44,** 441–460.

Busse, F.H. & Cuong, P.G., 1977. Convection in rapidly rotating spherical fluid shells, *Geophys. Astrophys. Fluid Dyn.,* **8,** 17–44.

Busse, F.H. & Simitev, R.D., 2006. Parameter dependences of convection-driven dynamos in rotating spherical fluid shells, *Geophys. Astrophys. Fluid Dyn.,* **100,** 341–361.

Christensen, U.R., 2002. Zonal flow driven by strongly supercritical convection in rotating spherical shells, *J. Fluid Mech.,* **470,** 115–133.

Christensen, U.R. & Wicht, J., 2007. Numerical Dynamo Simulations, in *Treatise on Geophysics*, ed. Schubert, G., Elsevier, Oxford.

Christensen, U.R., Olson, P.L. & Glatzmaier, G.A., 1999. Numerical modeling of the geodynamo: A systematic parameter study, *Geophys. J. Int.,* **138,** 393–409.

Conrath, B. & Gierasch, P., 1984. Global variation of the *para* hydrogen fraction in Jupiter's atmosphere and implications for dynamics on the outer planets, *Icarus,* **57,** 184–204.

Danilov, S. & Gurarie, D., 2002. Rhines scale and spectra of the β-plane turbulence with bottom drag, *Phys. Rev. E,* **65,** 067301.

Dormy, E., Soward, A.M., Jones, C.A., Jault, D., &, Cardin, P., 2004. The onset of convection in rotating spherical shells, *J. Fluid Mech.,* **501,** 43–70.

Evonuk, M. & Glatzmaier, G.A., 2004. 2D studies of various approximations used for modeling convection in the giant planets, *Geophys. Astrophys. Fluid Dyn.,* **98,** 241–255.

Fletcher, L.N. *et al.*, 2007. Characterizing Saturn's vertical temperature structure from Cassini/CIRS, *Icarus,* **189,** 457–478.

Gierasch, P.J. *et al.*, 2000. Observation of moist convection in Jupiter's atmosphere, *Nature,* **403,** 628–630.

Gilman, P.A., 1975. Linear simulations of Boussinesq convection in a deep rotating spherical shell, *J. Atmos. Sci.,* **32,** 1331–1352.

Gilman, P.A., 1977. Nonlinear dynamics of Boussinesq convection in a deep rotating shell—I, *Geophys. Astrophys. Fluid Dyn.,* **8,** 93–135.

Glatzmaier, G.A., 1984. Numerical simulations of stellar convective dynamos. I. The model and the method, *J. Comput. Phys.,* **55,** 461–484.

Guillot, T., 2005. The interiors of the giant planets: models and outstanding questions, *Annu. Rev. Earth Planet. Sci.,* **33,** 493–530.

Guillot, T., Stevenson, D.J., Hubbard, W. & Saumon, D., 2004. The interior of Jupiter, in *Jupiter, the Planet, Satellites and Magnetosphere*, eds Bagenal, F., Dowling, T.E. & McKinnon, W.B., Cambridge Univ. Press, Cambridge.

Hanel, R.A., Conrath, B.J., Herath, L., Kunde, V.G. & Pirraglia, J.A., 1981. Albedo, internal heat and energy balance of Jupiter—preliminary results of the Voyager infrared investigation, *J. geophys. Res.,* **86,** 8705–8712.

Hanel, R.A., Conrath, B.J., Kunde, V.G., Pearl, J.C. & Pirraglia, J.A., 1983. Albedo, internal heat and energy balance of Saturn, *Icarus,* **53,** 262–285.

Hide, R., 1966. Free hydrodynamic oscillations of the Earth's core and the theory of the geomagnetic secular variation, *Proc. Roy. Soc. A,* **259,** 615–647.

Heimpel, M.H. & Aurnou, J.M., 2007. Turbulent convection in rapidly rotating spherical shells: a model for equatorial and high latitude jets on Jupiter and Saturn, *Icarus,* **187,** 540–557.

Heimpel, M.H., Aurnou, J.M. & Wicht, J., 2005. Simulation of equatorial and high-latitude jets on Jupiter in a deep convection model, *Nature,* **438,** 193–196.

Ingersoll, A.P., 1976. Pioneer 10 and 11 observations and dynamics of Jupiter's atmosphere, *Icarus,* **29,** 245–253.

Ingersoll, A.P. & Pollard, D., 1982. Motion in the interiors and atmospheres of Jupiter and Saturn: scale analysis, anelastic equations, barotropic stability criterion, *Icarus,* **52,** 62–80.

Ingersoll, A.P. & Porco, C.C., 1978. Solar heating and internal heat flow on Jupiter, *Icarus,* **35,** 27–43.

Ingersoll, A.P. *et al.*, 1975. Pioneer 11 infrared radiometer experiment: the global heat balance of Jupiter, *Science,* **188,** 472–473.

Ingersoll, A.P. *et al.*, 2004. Dynamics of Jupiter's Atmosphere, in *Jupiter, the Planet, Satellites and Magnetosphere*, eds Bagenal, F., Dowling, T.E. & McKinnon, W.B., Cambridge Univ. Press, Cambridge.

Kono, M. & Roberts, P.H., 2001. Definition of the Rayleigh number for geodynamo simulation, *Phys. Earth planet. Inter.,* **128,** 13–24.

Kono, M. & Roberts, P.H., 2002. Recent geodynamo simulations and observations of the geomagnetic field, *Rev. Geophys.,* **40,** 1–53.

Liao, X., Zhang, K. & Feng, T., 2005. On convective instabilities and differential rotation in rapidly rotating stars: a new quasi-geostrophic approximation, *Astrophys. J.,* **631,** 518–528.

Liao, X., Feng, T. & Zhang, K., 2007. On the saturation and temporal variation of mean zonal flows: an implication for equatorial jets on the giant planets, *Astrophys. J.,* **666,** L41–L44.

Marcus, P.S. & Lee, C., 1998. A model for eastward and westward jets in laboratory experiments and planetary atmospheres, *Phys. Fluids,* **10,** 1474–1489.

Momary, T.W., Baines, K.H. & the Cassini/VIMS Science Team 2006. The zoology of Saturn: the bizarre features unveiled by the 5 micron eyes of Cassini/VIMS. AAS/Division for Planetary Sciences Meeting Abstracts, **38,** #11.21.

Nixon, C.A. *et al.*, 2007. Meridional variations of C_2H_2 and C_2H_6 in Jupiter's atmosphere from Cassini CIRS infrared spectra, *Icarus,* **188,** 47–71.

Ortiz, J.L., Orton, G.S., Friedson, A.J., Stewart, S.T., Fisher, B.M. & Spencer, J.R., 1998. Evolution and persistence of 5-micron hot spots at the Galileo probe entry latitude, *J. geophys. Res.,* **103,** 23 051–23 069.

Orton, G.S. & Yanamandra-Fisher, P.A., 2005. Saturn's temperature field from high resolution middle-infrared imaging, Science, **307,** 696–698.

Pirraglia, J.A., 1984. Meridional energy balance of Jupiter, *Icarus,* **59,** 169–176.

Roberts, P.H., 1968. On the thermal instability of a rotating-fluid sphere containing heat sources, *Phil. Trans. R. Soc. Lond. A* **263,** 93–117.

Sánchez Lavega, A. *et al.*, 2008. Depth of a strong jovian jet from a planetary-scale disturbance driven by storms, *Nature,* **451,** 437–440.

Simon-Miller, A.A., Conrath, B.J., Gierasch, P.J., Orton, G.S., Achterberg, R.K., Flasar, M.F. & Fisher, B.M., 2006. Jupiter's atmospheric temperatures: from Voyager IRIS to Cassini CIRS, *Icarus,* **180,** 98–112.

Sreenivasan, B. & Jones, C.A., 2006. Azimuthal winds, convection and dynamo action in the polar regions of planetary cores, *Geophys. Astrophys. Fluid Dyn.,* **100,** 319–339.

Stone, P.H., 1973. The dynamics of the atmospheres of the major planets, *Space Sci. Rev.,* **14,** 444–459.

Tritton, D.J., 1987. *Physical Fluid Dynamics*, Oxford Univ. Press, Oxford.

Vasavada, A.R. & Showman, A.P., 2005. Jovian atmospheric dynamics: an update after *Galileo* and *Cassini*, *Rep. Prog. Phys.,* **68,** 1935–1996.

Wicht, J., 2002. Inner-core conductivity in numerical dynamo simulations, *Phys. Earth planet. Int.,* **132,** 281–302.

Williams, G.P., 1985. Jovian and comparative planetary atmospheric modeling, *Adv. Geophys.,* **28,** 381–429.

Zhang, K., 1992. Spiralling columnar convection in rapidly rotating spherical fluid shells, *J. Fluid Mech.,* **235,** 535–556.